Geometry Analysis and Experimental Study for Vibration Damping of Rectangular Plate

Haining Sun, *Member, IEEE* and Shuzhi Sam Ge, *Fellow, IEEE*

***Abstract*—The effectiveness of vibration damping in rectangular plates depends not only on the control strategy but also on the geometric layout of the actuators. This study proposes a control-integrated geometry selection strategy that directly incorporates closed-loop control behavior. The geometry of cable-driven robots is analyzed by determining the number of cables required and identifying the positions of anchor points on the plate. A performance evaluation index is introduced, which simultaneously considers stabilization time, maximum cable force, and the number of cables. The selection strategy can provide optimized results tailored to diverse objectives, such as shorter stabilization time, reduced cable force, or fewer cables. Drawing on the patterns of the control input of the designed deep reinforcement learning-based controller, a new control law with customizable functions is developed, allowing for flexible output force modulation. It addresses the highly irregular nature of reinforcement learning-based control inputs and enhances the practicality in real-world applications. By combining the proposed control law with the geometry selection strategy, this study examines the effect of different geometric layouts on vibration damping in a rectangular plate under two distinct boundary conditions. A six-meter-scale experimental platform is constructed to assess sixteen geometric layouts under these two boundary conditions. Simulation and experimental results validate the practical feasibility of the geometry selection strategy for improving the vibration-damping effect in rectangular plates.**

***Index Terms*—Geometry analysis, vibration damping, cable-driven robot, rectangular plate.**

I. Introduction

EFFECTIVE vibration damping for large space structures requires not only efficient vibration control strategies but also optimized geometric layouts for the actuators [1]. Even when using the same control strategy, the damping effect can vary significantly depending on the geometries. Furthermore, the ideal geometric layout may differ depending on specific objectives, such as achieving shorter stabilization time or using fewer actuators.

Since the last century, researchers have been employing damping devices on the structures to reduce vibrations. In 1990, an inertial vibration absorber was installed at one end of a space structure to suppress vibrations [2]. Subsequent studies, such as [3] and [4], generally followed this trend by placing a single vibration absorber at the end of the structure. In [5], a different approach was adopted by installing two vibration absorbers at both ends of the structure to suppress the first two vibration modes. Despite this variation, the effect of different geometric layouts on vibration damping was not examined. Positioning actuators exclusively at the ends of the structures is common practice in many studies. For instance, in [6], a moment gyro was attached to the end of a cantilever beam. Similarly, in [7] and [8], magnetorheological and electrorheological fluid dampers were installed at the ends of the structures. However, this approach overlooks the potential benefits of placing actuators at different locations on the structure to enhance vibration damping. A slight deviation from this trend was seen in [9], where micro-thruster arrays were installed both in the middle and at the ends of the structure. However, this study did not include a performance evaluation index to optimize the geometry, leaving a gap in understanding how different actuator placements affect vibration damping in the structures.

Increasing awareness of how geometric layout affects vibration damping has prompted researchers to draw on past experience when determining actuator placements [10], [11]. In [12], a more quantitative approach was introduced by identifying the location of the maximum deformation in the structures and symmetrically placing actuators at this specific point. In [13], the optimized geometry layout for piezoelectric actuators was determined by identifying regions of the structure with higher average strains. A similar approach was proposed in [14] to determine the placement of collocated actuators based on the high position sensitivity of each vibration mode. However, these studies did not propose a clear performance evaluation index. To address this issue, researchers began using the observability and controllability of the system as indexes to determine the optimized geometric layout [15]. This approach was adopted in [16]-[19], where the positions of actuators and sensors were optimized based on modal controllability and observability. In [20], spatial and modal controllability concepts were employed to optimally place collocated piezoelectric actuator-sensor pairs. Differently, the tip displacement was introduced to the index in [21] to obtain the optimal layout for a single moment gyro. In [22], researchers formulated an objective function to quantify the effectiveness of elastic mode suppression and

Manuscript received xxx; revised xxx; accepted xxx. Date of publication xxx; date of current version xxx. This work was supported in part by Singapore RIE2025 Manufacturing, Trade and Connectivity (MTC) Industry Alignment Fund – Pre-Positioning (IAF-PP) grant M22K4a0044 and the Ministry of Education, Singapore, under its Research Centre of Excellence award to the Institute for Functional Intelligent Materials (I-FIM, project No. EDUNC-33-18-279-V12). *(Corresponding author: S. S. Ge)*.

H. Sun is with the Singapore Institute of Manufacturing Technology, Agency for Science, Technology and Research (A*STAR), 138634, Singapore (e-mail: sunhn@simtech. a-star.edu.sg).

S. S. Ge is with the Institute for Functional Intelligent Materials, and Department of Electrical and Computer Engineering, National University of Singapore, 117583, Singapore (e-mail: samge@nus.edu.sg).

The supplementary material includes a video showing the experimental platform, along with figures corresponding to the simulations.

determined the optimal geometric layout by minimizing this function. In [23], the H_2-norm of the closed-loop transfer matrix was introduced as part of the optimization index for actuator placement. Additionally, in [24], the optimal locations of patch actuators were determined by maximizing the fundamental frequency, thereby avoiding resonance at excitation frequencies.

In summary, existing studies [10]-[29] primarily used several principles to determine the optimized geometric layout of actuators, including high average strains, structural deflection, energy dissipation, controllability, observability, frequency, and spill-over effects. However, the optimization procedures in these studies overlooked a key aspect: the limit of control inputs, which can be essential in certain applications. For instance, long-span space structures have a threshold for the control force they can tolerate, and exceeding this limit could result in structural damage. Thus, determining the optimized geometric layout of actuators requires balancing the vibration damping effect with the constraints on control inputs. Additionally, the number of actuators is another critical factor, especially given the mass, volume, and power constraints in aerospace applications. To the best of our knowledge, the simultaneous consideration of stabilization time, constrained control inputs, and the number of actuators in a unified performance metric for geometry selection has not been reported in previous studies.

Research on vibration damping in the structures has predominantly focused on clamped-free-free-free (CFFF) or simply supported boundary conditions [3]-[9], [12]-[21], [23]-[35], with the boundary conditions of space structures often assumed to be similar. This assumption arises from the fact the main body of spacecraft, such as satellites or space stations, is typically much more massive than their appendages. However, for large-span space structures whose mass may exceed that of the spacecraft's main body, the boundary condition in microgravity would more closely resemble a free-free-free-free (FFFF) boundary. Only limited studies [10], [11], [22] investigated the effects of vibration damping under the FFFF condition. However, in [10], [11], [22], the optimized geometric layouts were determined without fully integrating stabilization time, control input limits, and the number of actuators. This gap motivates us to explore the impact of different geometric layouts on vibration damping in the structures, particularly under both CFFF and FFFF boundary conditions. Given the huge workspace of cable-driven robots (CDRs) and the lightweight nature of cables [36], [37], we use CDRs as damping actuators for vibration damping of the structures (see Fig. 1).

The main contributions of this work are as follows:

1) A complete geometry selection strategy integrating closed-loop control behavior is proposed, unlike prior works [18], [25], [28], [29], [31] which did not consider this integration during geometry selection. This work also simultaneously considers stabilization time, control input constraints, and the number of cables, offering geometries tailored to diverse control objectives such as achieving faster stabilization or reducing cable forces.
2) Drawing on the characteristics of the control input of the designed deep reinforcement learning-based controller, a new control law with customizable functions is developed, allowing for flexible output force modulation and ensuring effective vibration damping.
3) Under CFFF and FFFF boundary conditions, 16 distinct geometric layouts are constructed on a six-meter-scale experimental platform to assess their impact on vibration damping. The optimized geometric layouts for different control objectives demonstrated their obvious advantages in the experiments, which verified the practical feasibility of the selection strategy.

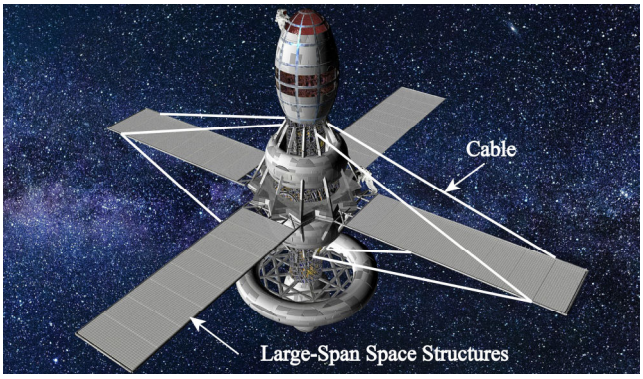

Fig. 1. Vibration damping for large-span space structures.

The rest of this article is organized as follows: Section II describes the system model. Section III introduces the control law. The geometry selection strategy, along with the simulation and experimental results, is discussed in Sections IV and V, respectively. Section VI gives the conclusion.

II. System Model

The system model (see Fig. 2) includes a rectangular plate and a CDR with m cables. The ith cable is connected to the plate at anchor point B_i (i = 1, 2, …). Using the finite element method, the plate could be discretized into $(n_w\text{-}1) \times (n_l\text{-}1)$ rectangular elements. Each element has four nodes, and each node has three degrees of freedom: out-of-plane displacement (along z-axis) and two rotations about the x-axis and y-axis. This element is one of the plate finite elements; although it is planar, it can model out-of-plane displacement and bending [38], [39]. The following assumption is made in this study:

Assumption 1: Each cable in the CDR is simplified as a massless linear elastic model. The deformation of the rectangular plate follows the Kirchhoff's law.

As shown in Fig. 2, the mesh consists of $n_w \times n_l$ nodes (n_w and n_l are positive integers). Numbering starts at one in the lower left corner, increasing from left to right and bottom to top, with the final node being numbered $n_w \times n_l$.

According to [38], [39] the element stiffness matrix $\boldsymbol{K}_e$ and mass matrix $\boldsymbol{M}_e$ could be expressed as:

$$\boldsymbol{K}_e = \frac{Ed^3}{12(1-\nu^2)} \int_{V^e} \boldsymbol{B}^{\mathrm{T}} \begin{bmatrix} 1 & \nu & 0 \\ \nu & 1 & 0 \\ 0 & 0 & (1-\nu)/2 \end{bmatrix} \boldsymbol{B} dV \tag{1}$$

$$\boldsymbol{M}_e = \int_{V^e} \rho \boldsymbol{N} \boldsymbol{N}^T dV \tag{2}$$

where the shape function matrix $\boldsymbol{N}$ and the gradient matrix $\boldsymbol{B}$ are given in the supplementary material. E, ν, ρ, and d denote the Young's modulus, Poisson's ratio, density and thickness of

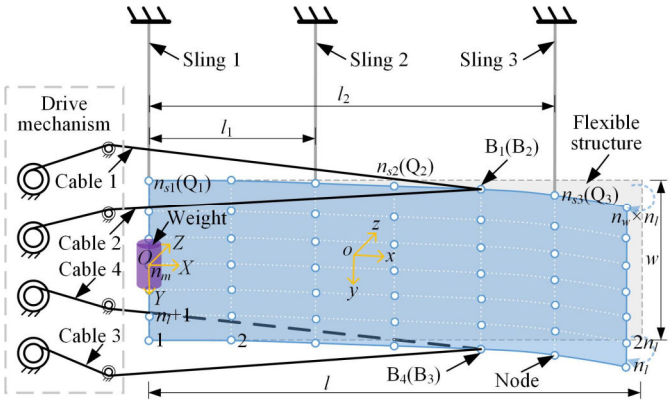

Fig. 2. A thin rectangular plate with a *m*-cable CDR.

the plate, respectively.

The main body of the satellite is represented by attaching a weight M_l to one side of the rectangular plate. Assuming the weight is attached to node n_m, the mass matrix $\boldsymbol{M}_{em}$ of this element can be expressed as:

$$\boldsymbol{M}_{em} = \int_{V^e} \rho \boldsymbol{N}\boldsymbol{N}^{\mathrm{T}} dV + M_l \boldsymbol{N}\boldsymbol{N}^{\mathrm{T}} \tag{3}$$

Using the direct stiffness method [39], the global mass matrix $\boldsymbol{M}$ and stiffness matrix $\boldsymbol{K}$ of the plate, as well as surface force matrix $\boldsymbol{u}_F$ are assembled from (1), (2), (3), and (S7) (refer to [38], [39] and the supplementary material). To model the damping matrix $\boldsymbol{C}$, the following assumption is made:

Assumption 2: Rayleigh damping is assumed for the plate, i.e., $\boldsymbol{C} = \varsigma_1 \boldsymbol{M} + \varsigma_2 \boldsymbol{K}$, where $\varsigma_1 > 0$ and $\varsigma_2 > 0$.

Then, the dynamic model of the system shown in Fig.2 can be expressed as:

$$\boldsymbol{M}\ddot{\boldsymbol{z}}(t) + \boldsymbol{C}\dot{\boldsymbol{z}}(t) + \boldsymbol{K}\boldsymbol{z}(t) = \boldsymbol{u}_F(t) \tag{4}$$

where $\boldsymbol{z}$ is the displacement vector of all nodes of the plate.

III. Controller Design

Since the geometry selection strategy integrates closed-loop control behavior, the design of a control law is essential. A deep reinforcement learning-based controller (DRLBC) is first designed, from which the underlying vibration damping logic of the trained agent is identified. Inspired by this logic, a new control law with customizable functions is developed to address some limitations inherent in the DRLBC. Moreover, the vibration damping effect of this new control law is compared with that of the model predictive control (MPC) and the fuzzy PI controller (see supplementary material).

A. Design of the DRLBC

Fig. 3 shows the control block diagram of the DRLBC. After observing the tip displacement and velocity of the plate, the trained agent outputs the desired cable forces. The detailed steps for training such an effective agent are as follows:

Step 1 Environment interaction and data storage: The agent generates a control action (cable force) $a_t = G_1(s_t)$ through the actor network G_1, where t denotes the time step and the network structure of G_1 is shown in Fig. 4. The plate generates the corresponding state s_{t+1} (tip displacement and velocity) under the action of a_t and returns a reward r_t based on the resulting state of the plate. This transition tuple (s_t, a_t, r_t, s_{t+1}) is stored in a replay buffer *Rb*.

Step 2 Sampling from the replay buffer: A mini-batch of

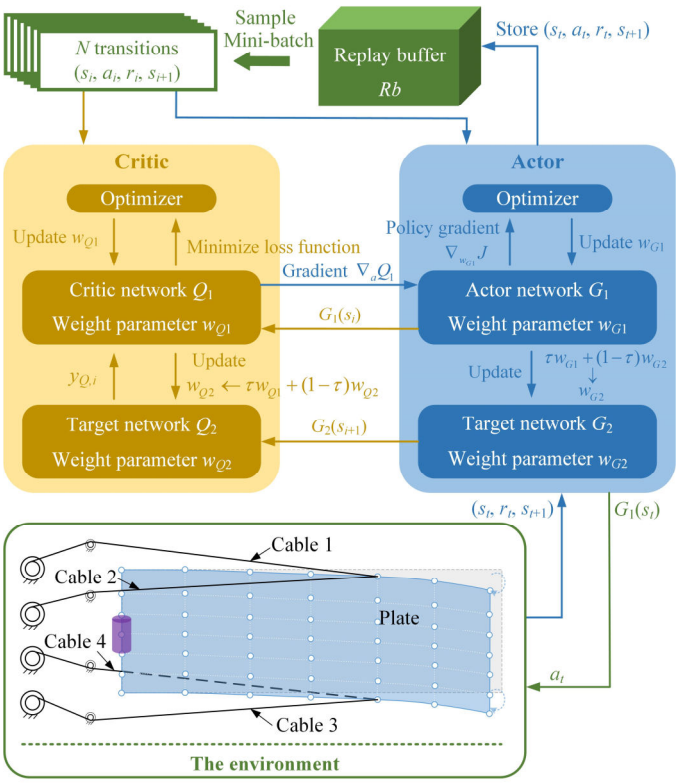

Fig. 3. Control block diagram of the DRLBC.

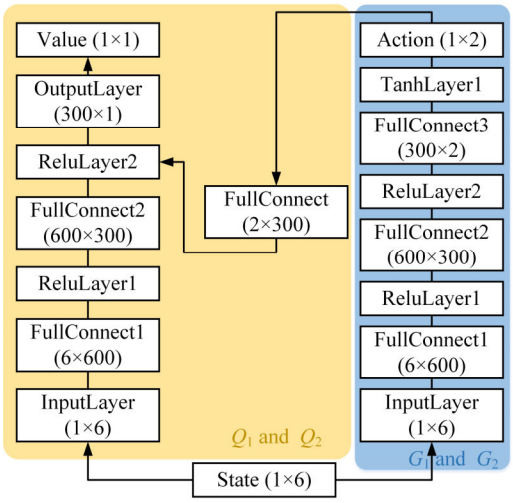

Fig. 4. Network structure.

transition samples (N=128) is randomly selected from the replay buffer. Each sample contains a tuple (s_i, a_i, r_i, s_{i+1}) denoting the past interaction data, where $i = 1, 2, \ldots N$.

Step 3 Critic network Q_1 update: To train the critic network, a target Q-value (see (5)) is computed for each sampled tuple (s_1, a_1, r_1, s_2), …, (s_i, a_i, r_i, s_{i+1}), … from the replay buffer.

$$y_{Q,i} = r_i + \gamma Q_2\left(s_{i+1}, G_2(s_{i+1})\right) \tag{5}$$

where $\gamma = 0.9$ is the discount factor for future rewards. Q_2 and G_2 are the target critic and target actor networks, respectively. Q_2 and G_2 share the network structure as Q_1 and G_1, respectively, as shown in Fig. 4. $Q_2(s_{i+1}, G_2(s_{i+1}))$ is the target critic network's estimate of the next state's return.

Using the target Q-value and predicted value $Q_1(s_i, a_i)$, the

loss function L_Q for the critic network Q_1 is defined as the mean squared error:

$$L_Q = (1/N)\sum_{i}^{N}\left(y_{Q,i} - Q_1\left(s_i, G_1(s_i)\right)\right)^2 \tag{6}$$

The critic network Q_1 is updated by minimizing this loss using gradient descent to adjust its learnable parameters w_{Q_1}.

Step 4 Actor network G_1 update: The actor network G_1 is responsible for learning a deterministic policy that maps states s_t to continuous actions a_t, i.e., the cable forces applied to the plate. G_1 is trained to maximize the critic network's estimated Q-value ($Q_1(s_i, G_1(s_i))$) with respect to the actions it proposes:

$$J(G_1) = \mathbb{E}_{s_i \sim Rb}\left[Q_1\left(s_i, G_1(s_i)\right)\right] \tag{7}$$

where $Q_1(s_i, G_1(s_i))$ is the critic network's estimate of the return for taking the action a_i proposed by the actor network G_1. The expectation is taken over a mini-batch of states sampled from the replay buffer Rb. The gradient of the objective function J with respect to the actor network's parameters w_{G_1} is computed using the chain rule of differentiation (via backpropagation [40]):

$$\nabla_{w_{G1}} J \approx (1/N)\sum_{i}^{N}\left[\nabla_{a_i} Q_1\left(s_i, G_1(s_i)\right)\nabla_{w_{G1}} G_1(s_i)\right] \tag{8}$$

where $\nabla_{a_i} Q_1(s_i, a_i)$ is the gradient of the critic network's output with respect to the action (how Q_1 changes if action changes). $\nabla_{w_{G1}} G_1(s_i)$ is the gradient of the actor network's action output with respect to its own parameters. Together, this gives the direction in which to update the actor network so that it proposes actions that lead to higher Q-values (i.e., higher expected returns).

Step 5 Target network update: The target networks Q_2 and G_2 are updated using soft updates:

$$\begin{cases} w_{Q2} \leftarrow \tau_1 w_{Q1} + (1-\tau_1) w_{Q2} \\ w_{G2} \leftarrow \tau_2 w_{G1} + (1-\tau_2) w_{G2} \end{cases} \tag{9}$$

where $\tau_1 = 1\times10^{-3}$ and $\tau_2 = 1\times10^{-4}$ are the learning rate.

The total reward r_t at each time step t is composed of four components ε_1, ε_2, ε_3, ε_4 ($r_t = \varepsilon_1 + \varepsilon_2 + \varepsilon_3 + \varepsilon_4$). Each penalizes or encourages certain behavior to ensure vibration damping.

$$\varepsilon_1 = \begin{cases} 10, & |v_{tip}| \le 15 \text{ mm/s} \\ -1, & |v_{tip}| > 15 \text{ mm/s} \end{cases} \tag{10}$$

$$\varepsilon_2 = \begin{cases} 0, & 0 \text{ N} \le u(t) \le 15 \text{ N} \\ -100, & u(t) < 0 \text{ N or } u(t) > 15 \text{ N} \end{cases} \tag{11}$$

$$\varepsilon_3 = \begin{cases} 0, & |z_{tip}| \le 150 \text{ mm} \\ -100, & |z_{tip}| > 150 \text{ mm} \end{cases} \tag{12}$$

$$\varepsilon_4 = \begin{cases} 20, & \text{-5 mm} \le z_{tip} \le 5 \text{ mm} \\ 10, & 5 \text{ mm} \le |z_{tip}| \le 15 \text{ mm} \\ 0, & 15 \text{ mm} \le |z_{tip}| \le 50 \text{ mm} \\ \text{-5}, & 50 \text{ mm} \le |z_{tip}| \le 80 \text{ mm} \\ \text{-10}, & 80 \text{ mm} \le |z_{tip}| \le 100 \text{ mm} \\ \text{-20}, & 100 \text{ mm} \le |z_{tip}| \end{cases} \tag{13}$$

where z_{tip} and v_{tip} denote the tip displacement and velocity of the plate, respectively.

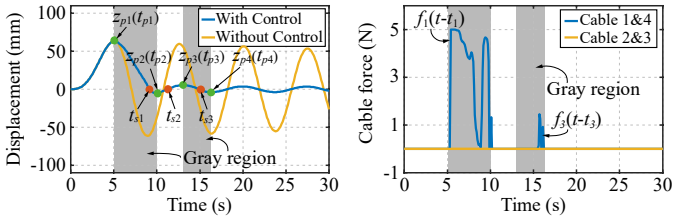

Fig. 5. Results using the designed DRLBC with initial deviation of 64 mm.

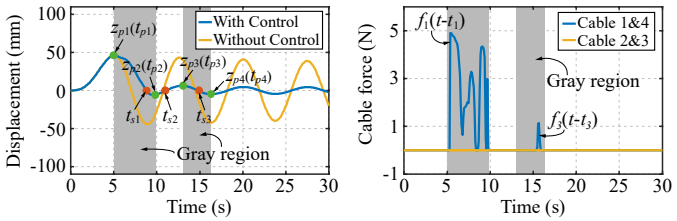

Fig. 6. Results using the designed DRLBC with initial deviation of 46 mm.

Under DRLBC control, the tip displacement of the plate and cable forces for initial deviations of 64 mm and 46 mm are shown in Figs. 5 and 6. For initial deviations of 64 mm and 46 mm, the stabilization times under DRLBC control are 13.6 s and 13.7 s, with corresponding maximum cable forces of 5.0 N and 4.9 N, respectively. These results indicate that the DRLBC achieves effective vibration damping. However, they also reveal several limitations of the DRLBC: 1) The patterns of cable forces are complex and highly irregular, making them difficult to track accurately. 2) Only one side of the cables contributes to the force output, while the other side remains inactive, indicating that there is still room to reduce the stabilization time. 3) As the initial deviation decreases, the stabilization time does not significantly improve.

B. Analysis of the vibration damping logic of the DRLBC

Despite these limitations of the DRLBC, its underlying logic for effective vibration damping still warrants further investigation. As shown in Fig. 5 and Fig. 6, one notable feature of the DRLBC is the discontinuity of force output, which means that the DRLBC outputs force in discrete time intervals, concentrating it over a specific duration. In the displacement curve under DRLBC control (shown in blue), for the sake of illustration, let's highlight the time intervals between the time points corresponding to two adjacent local extrema as gray-shaded regions. It is not difficult to see that the discontinuous outputs of DRLBC are all distributed within these gray-shaded regions. For clarity, we focus on the first interval (t_{p1}, t_{p2}) as an example, during which the anchor point B_i transitions from one relative extremum to another. Referring to the coordinate system $\{O\}$ in Fig. 2, it can be seen that during the interval (t_{p1}, t_{p2}), the anchor point moves toward the negative direction of the Z-axis, where Cables 2 and 3 are located. Together with Fig. 5 and Fig. 6, it can be observed that during this interval Cables 1 and 4 exactly output force, while Cables 2 and 3 remain inactive. Consequently, the angle between the force direction of Cables 1 and 4 and the velocity of the anchor point exceeds 90°, resulting in negative work by the output forces and thus reducing the vibration energy of the plate. It can be deduced that the underlying principle of DRLBC is to achieve vibration damping by continuously dissipating the vibration energy of the plate. Inspired by this concept, we have designed a new

control law that retains the vibration damping logic of DRLBC while addressing its limitations.

C. Design of a new control law inspired by the DRLBC

Let's define a subinterval within the gray-shaded region (t_{pr}, t_{pr+1}) as (t_r, $t_r+\Delta t_r$), where r = 1, 2, … (see Fig. 7). That is to say, $t_{pr} \le t_r$ and $t_r+\Delta t_r \le t_{pr+1}$. t_r represents the triggering time of the r-th discontinuous output of the control law. The new control law $u(t)$ can be designed as:

$$u(t)=\begin{cases} f_r\left(t-t_r\right), t\in\left(t_r, t_r+\Delta t_r\right) \\ 0\ , t\in\left[t_r+\Delta t_r, t_{r+1}\right] \end{cases}, r=1,2,... \tag{14}$$

where $f_r(t\text{-}t_r)$ is a bounded function defined on the open interval (t_r, $t_r+\Delta t_r$), with $f_r(t\text{-}t_r) \ge 0$. There exists a positive scalar ε_r such that $max(f_r(t\text{-}t_r)) \le \varepsilon_r$. t_{pr} is the time point corresponding to the peaks and valleys z_{pr} of the displacement curve. For instance, t_{p1} is the time point of the first relative extremum z_{p1} on the displacement curve. The customizable component lies in the functional form of $f_r(t\text{-}t_r)$, which can be flexibly specified—for example, as a parabolic, trigonometric, or linear function. The cable forces F_1, F_2, F_3, and F_4 are:

$$\begin{cases} F_1=F_4=u(t), F_2=F_3=0, \text{ for } z_{pr}>0 \\ F_2=F_3=u(t), F_1=F_4=0, \text{ for } z_{pr}<0 \end{cases} \tag{15}$$

where z_{pr} represents the displacement of the r-th relative extremum on the vibration curve.

In Fig. 7, we use the first interval (t_1, $t_1+\Delta t_1$) as an example to explain the vibration damping logic of the new control law in (14). This interval is a subset of the broader range (t_{p1}, t_{p2}), which is the same as the gray-shaded region shown in Figs. 5 and 6. Within (t_1, $t_1+\Delta t_1$), the control input $u(t)$ in (14) is generated based on the function $f_1(t\text{-}t_1)$. During this interval, anchor points B_i move toward the negative direction of the Z-axis, where Cables 2 and 3 are located. Based on (14) and (15), Cables 1 and 4 output force $f_1(t\text{-}t_1)$, whereas Cables 2 and 3 do not exert any force. Referring to the coordinate system $\{O\}$ in Fig. 2, the side where Cables 1 and 4 are located corresponds to the positive direction of the Z-axis. Therefore, the angle between the direction of cable forces (Cables 1 and 4) and the velocity of the anchor point exceeds 90°, causing the output forces of Cables 1 and 4 to perform negative work, similar to the underlying vibration damping logic of the DRLBC, thereby reducing the vibration energy of the plate.

Theorem 1: The control input and cable force determined by (14) and (15) can ensure the stability of the control system and continuously dissipate the vibration energy of the plate.

Proof: First, the following useful lemma is introduced:

Lemma 1 (in [41]): A thin plate's vibration energy consists of strain energy L_{strain}, as well as kinetic energy $L_{kinetic}$, whose expressions are as follows:

$$L_{strain}=\frac{1}{2}\iint_{\Sigma}\frac{Ed^3}{12(1-\nu^2)}\left(\left(\frac{\partial^2 z}{\partial X^2}\right)^2+\left(\frac{\partial^2 z}{\partial Y^2}\right)^2 +2(1-\nu)\left(\frac{\partial^2 z}{\partial X\partial Y}\right)^2+2\nu\frac{\partial^2 z}{\partial X^2}\frac{\partial^2 z}{\partial Y^2}\right)dXdY. \tag{16}$$

$$L_{kinetic}=\frac{1}{2}\iint_{\Sigma}\rho d\left(\frac{\partial z}{\partial t}\right)^2 dXdY. \tag{17}$$

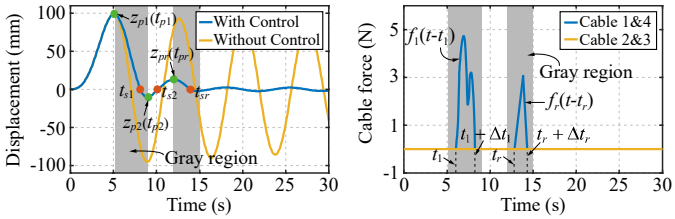

Fig. 7. Tip displacement of the plate and output force of the control law.

$$L(t)=\frac{1}{2}\iint_{\Sigma}\frac{Ed^3}{12(1-\nu^2)}\left(2\nu\frac{\partial^2 z}{\partial X^2}\frac{\partial^2 z}{\partial Y^2}+\left(\frac{\partial^2 z}{\partial X^2}\right)^2+\left(\frac{\partial^2 z}{\partial Y^2}\right)^2 +2(1-\nu)\left(\frac{\partial^2 z}{\partial X\partial Y}\right)^2\right)dXdY+\frac{1}{2}\iint_{\Sigma}\rho d\left(\frac{\partial z}{\partial t}\right)^2 dXdY \tag{18}$$

Let's consider a Lyapunov function candidate as shown in (18). According to *Lemma 1*, the Lyapunov function in (18) represents the total vibration energy of the plate, and therefore, $L(t) \ge 0$. Considering the control input's characteristic shown in (14), we analyze the stability of the control system under two different scenarios.

1) $u(t) = 0$, $t \in [t_r+\Delta t_r, t_{r+1}]$

During the time interval $[t_r+\Delta t_r, t_{r+1}]$, the cable forces remain zero, and only the structural damping dissipates the vibration energy. Let the Lyapunov function values at times t_1 and t_2 (where $t_2 = t_1+\Delta t$) be $L(t_1)$ and $L(t_2)$, respectively. Δt is a tiny time interval. Let the work done by the damping be denoted as L_d. Since the damping force always opposes to the vibration velocity of the plate, $L_d < 0$ is always satisfied. According to the law of conservation of energy, we have:

$$L(t_2)=L(t_1)+L_d \tag{19}$$

When computing the derivative of the Lyapunov function $L(t)$ at time t_1, we obtain:

$$\dot{L}(t_1)=\lim_{\Delta t\to 0}\frac{L(t_2)-L(t_1)}{\Delta t}<0 \tag{20}$$

2) $u(t) = f_r(t\text{-}t_r)$, $t \in (t_r, t_r+\Delta t_r)$

Let the work performed by the cable force be denoted as L_c. Since the interval (t_r, $t_r+\Delta t_r$) is contained within the larger interval (t_{pr}, t_{pr+1}), the angle between the direction of the cable force and the anchor point's velocity exceeds 90°. Therefore, it follows that $L_c < 0$. According to the law of conservation of energy, we have:

$$L(t_2)=L(t_1)+L_d+L_c \tag{21}$$

By taking the derivative of the Lyapunov function $L(t)$ at time t_1, we obtain:

$$\dot{L}(t_1)=\lim_{\Delta t\to 0}\frac{L(t_2)-L(t_1)}{\Delta t}=\lim_{\Delta t\to 0}\frac{L_d+L_c}{\Delta t}<0 \tag{22}$$

Lemma 2: Constraint (23) for $f_r(t\text{-}t_r)$ guarantees that cable forces do not perform excessive work, preventing an increase in vibration energy.

$$\int_{t_r}^{t_r+\Delta t_r}2f_r\left(t-t_r\right)\sin(\theta_m)\frac{\partial z(X,Y,t)}{\partial t}dt \le\frac{1}{2}\iint_{\Sigma}\rho d\left(\frac{\partial z(X,Y,t_{sr})}{\partial t}\right)^2 dXdY,\ r=1,2,... \tag{23}$$

where $\theta_m = max(\theta_i)$, i = 1, 2, …, m.

Proof: Without loss of generality, we focus on the first

interval (t_1, $t_1+\Delta t_1$) as an illustrative case. At t_{p1}, the anchor points reach the relative extremum, where the function $L(t_{p1})$ consisting solely of strain energy. When cable forces stay at zero, the vibration energy of the plate progressively decreases from t_{p1} to t_{s1} under the influence of damping. Define L_d^* as the work performed by damping force. Then, we have:

$$L(t_{s1}) = L(t_{p1}) + L_d^* \tag{24}$$

where $L(t_{s1})$ represent the vibration energy at t_{s1}.

When the cable force is not zero, especially when the vibration energy is very low, it is crucial to ensure that the work performed by cable forces does not increase vibration energy $L(t_{s1})^*$ (see (25)). In other words, the plate must be capable of reaching the equilibrium position.

$$L(t_{s1})^* = L(t_{p1}) + L_{dc}^* - \left|L_c^*\right| \geq 0 \tag{25}$$

where L_c^* and L_{dc}^* represent the work done by the cable force and the damping force, respectively, when the control input is non-zero. L_c^* can be expressed as:

$$L_c^* = \int_{t_r}^{t_r+\Delta t_r} 2 f_r\left(t-t_r\right)\sin(\theta_m)\frac{\partial z(X,Y,t)}{\partial t}dt. \tag{26}$$

Non-zero cable forces progressively dissipate the vibration energy of the plate, thus decreasing the vibration velocity. Therefore, we have $|L_{dc}^*| \leq |L_d^*|$. Nonetheless, to obtain a more conservative value for $f_r(t-t_r)$, we can assume $L_{dc}^* = L_d^*$. At t_{s1}, $L(t_{s1})$ includes only kinetic energy when the plate reaches the equilibrium position. Combining (17), (24) and (25) yields:

$$\left|L_c^*\right| \leq \frac{1}{2}\iint_{\Sigma}\rho d\left(\frac{\partial z(X,Y,t_{s1})}{\partial t}\right)^2 dXdY \tag{27}$$

By combining (26) and (27), the constraints on $f_r(t-t_r)$ in (23) could be obtained. As of now, *Theorem 1* has been proved.

For the experiments in Section V, the function $f_r(t-t_r)$ is chosen as a constant function, expressed as $f_r(t-t_r)=\eta_r$, where r = 1, 2, …. The control input in (14) can be rewritten as:

$$u(t) = \begin{cases} \eta_r,\ t \in \left(t_r, t_r+\Delta t_r\right) \\ 0\ ,\ t \in \left[t_r+\Delta t_r, t_{r+1}\right] \end{cases},\ r = 1,2,... \tag{28}$$

where η_r is expressed as:

$$\eta_r = \begin{cases} \sigma_1,\ \ \left|z_{pr}\right| > \xi_1 \\ \sigma_k,\ \ \xi_{k-1} \geq \left|z_{pr}\right| > \xi_k \\ ... \\ \sigma_q,\ \ \left|z_{pr}\right| \leq \xi_{q-1} \end{cases},\ k = 1,2,...,q \tag{29}$$

where scalars σ_1, …, $\sigma_q \geq 0$ and ξ_1, …, $\xi_{q-1} > 0$. The set $\{\xi_1, …, \xi_{q-1}\}$ represents the displacement of a series of peaks and valleys of the vibration curve, which is a subset of $\{z_{p1}, z_{p2}, …\}$. In (29), we take one segment ($\xi_{k-1} \geq |z_{pr}| > \xi_k$) as an example to illustrate. Assuming that the time corresponding to ξ_k is t_{pr}, it can be observed in Fig. 5 that the plate will reach the equilibrium position at time t_{sr}. Based on (23), the value range of σ_k can then be determined as follows:

$$\sigma_k \leq \frac{\frac{1}{2}\iint_{\Sigma}\rho d\left(\frac{\partial z(X,Y,t_{sr})}{\partial t}\right)^2 dXdY}{2\sin(\theta_m)\int_{t_r}^{t_r+\Delta t_r}\frac{\partial z(X,Y,t)}{\partial t}dt}. \tag{30}$$

IV. Geometry Selection Strategy

A. Performance Index

The performance index P_I in (31) simultaneously considers stabilization time, control input constraints, and the number of cables. To incorporate the three key factors into a single performance index, we first converted and normalized them to solve the problem of their different units and scales, as shown in (32). In practice, the importance of the three factors may vary depending on specific objectives. For example, stabilization time may be critical in some cases, while reducing maximum cable force may take precedence in others. To accommodate this, we introduce weighting coefficients via vector $\boldsymbol{W}$ in (31). These coefficients, parameterized using trigonometric functions (cosines and sines), allow flexible adjustment of the performance index to align with the objectives. Many indices—such as controllability, frequency response, structural deflection, and spill-over effects—have been used in the literature [18], [25], [28], [29], and [31], each providing valuable insights for specific objectives. For space structures, it is particularly important to consider not only stabilization time but also maximum cable force and the number of cables. This is because excessive external force can damage such structures, and increasing the number of cables results in more drive mechanisms and a more complex system. Therefore, we integrate all the three factors. Moreover, they are closely related to closed-loop control behavior. Incorporating these behaviors ensures that the optimized geometric layout is well-matched with the control law.

$$P_{I,i} = \left\|\boldsymbol{W} \oplus \boldsymbol{P}_{I,i}\right\|, i = 1,2,... \tag{31}$$

where $\boldsymbol{W} = [\cos(\alpha),\ \sin(\alpha)\cos(\beta),\ \sin(\alpha)\sin(\beta)]^T$ represents a normalized weighting vector in a 3D Cartesian coordinate system $\{O_C\}$, and $\alpha, \beta \in [0,\ \pi/2]$ (see Fig. S1 in the supplementary material). $\boldsymbol{P}_{I,i}$ is defined as follows:

$$\boldsymbol{P}_{I,i} = \left[\frac{t_{di}}{\sqrt{t_{d1}^2+\cdots+t_{dh}^2}},\ \frac{F_{ci}}{\sqrt{F_{c1}^2+\cdots+F_{ch}^2}},\ \frac{N_{ci}}{\sqrt{N_{c1}^2+\cdots+N_{ch}^2}}\right]^T \tag{32}$$

For the ith geometry (i = 1, 2, …, h), t_{di}, F_{ci} and N_{ci} represent the stabilization time, the maximum cable force, and the number of cables, respectively. Here, h denotes the total number of the geometries. The operator symbol $\oplus$ is defined as:

$$\boldsymbol{W} \oplus \boldsymbol{P}_{I,i} = \left[\boldsymbol{W}(1)\boldsymbol{P}_{I,i}(1),\ \ \boldsymbol{W}(2)\boldsymbol{P}_{I,i}(2),\ \ \boldsymbol{W}(3)\boldsymbol{P}_{I,i}(3)\right]^T \tag{33}$$

where $\boldsymbol{W}(j)$ and $\boldsymbol{P}_{I,i}(j)$ denote the jth component of the vector $\boldsymbol{W}$ and $\boldsymbol{P}_{I,i}$, respectively, with j=1, 2, 3.

In Fig. S1, we assign $\boldsymbol{P}_{I,i}(1)$, $\boldsymbol{P}_{I,i}(2)$, and $\boldsymbol{P}_{I,i}(3)$ in (32) as the labels for three axes of the Cartesian coordinate system $\{O_P\}$. These values correspond to the stabilization time, the maximum control force, and the number of cables, respectively. Lower values for the ith geometric layout indicate more desirable outcomes: shorter stabilization time, reduced cable force, or fewer cables.

B. Geometry Selection

1) Generation of predefined anchor points

Before the cables are connected to the plate, we refer to all potential locations for cable attachment as "predefined anchor points." These predefined anchor points become actual "anchor points" only when cables are physically connected to

the plate. The first stage of the geometry selection strategy involves generating a large set of discrete predefined anchor points, which will later be combined with the cable arrangement to form distinct geometric layouts.

The parameters of the plate, including its dimensions (l×w×d), density (ρ), damping coefficient (ς_1, ς_2), Young's modulus (E), and Poisson's ratio (v), as well as the maximum allowable number of cables must first be defined.

The user also needs to define a set of dimensional parameters that determine the relative positions between the predefined anchor points. For example, if the predefined anchor points are neatly arranged in a grid pattern, similar to the nodes in Fig. 2, the gaps Δl and Δw between adjacent predefined anchor points along the X-axis and Y-axis, respectively, serve as the dimensional parameters.

The arrangement of the predefined anchor points can be symmetrical, with specific symmetry rules clearly defined. For rectangular plates with non-negligible width w, an asymmetric arrangement of predefined anchor points about the X-axis can induce torsional vibration modes around the X-axis. In this paper, we specify that predefined anchor points must either be positioned directly on the X-axis or, if not, have a symmetrical counterpart across the X-axis.

2) Cable arrangement

In this stage, the task is to connect the cables to the predefined anchor points identified in the first stage, thereby creating complete geometric layouts. We follow the principle of symmetry when generating cable arrangements: for cables on the same side of the plate, their anchor points with the plate should be symmetrical about the X-axis, except for the anchor points that are positioned directly on the X-axis. This helps to reduce the risk of inducing torsional vibration modes. Additionally, we specify that each cable is uniquely matched to one predefined anchor point.

3) Preliminary screening

By integrating the two stages described above, we can generate different geometric layouts of the CDR, consisting of the positions of predefined anchor points on the plate and corresponding cable arrangements. Let S_{original} be a set whose members are the generated geometric layouts Si: $S_{\text{original}} = \{S1, S2, Si\ldots\}$. For each geometry layout Si, we use the designed control law (14), (15) and Wilson method [42] to solve the complete vibration damping process and obtain the values of t_{di} and F_{ci}. Let's introduce a positive scalar δ as the criterion for the end of vibration, with t_{di} determined by:

$$\begin{aligned} &\text{minimize} \quad t_{di} \\ &\text{subject to} \quad \left| z(X,Y,t) \right|_{t\in[t_{di},\,\infty)} \le \delta \end{aligned} \tag{34}$$

where $t_{di} \in [0,\ \infty)$, $X = l$, and $Y = 0$.

Then, we can obtain:

$$F_{ci} = \max_{t\in[0,t_{di}]} u(t) \tag{35}$$

Based on the stabilization time and the maximum cable force, users can define two corresponding evaluation criteria, δ_t and δ_F, to complete a preliminary screening of geometric layouts. Only layouts that satisfy the conditions $t_{di} \le \delta_t$ and $F_{ci} \le \delta_F$ can proceed to the next stage. Let S_{pre} be a set whose members are the selected geometric layouts:

$$S_{pre} = \left\{ Si \in S_{original} \;\middle|\; t_{di} \le \delta_t \text{ and } F_{ci} \le \delta_F \right\} \tag{36}$$

4) Determining the optimized geometry

The preferred geometric layout of the CDR is the one with the minimal performance index $P_{I,i}$ as defined in (31). The minimization problem can be formulated as follows:

$$\begin{aligned} &\text{minimize} \quad P_{I,i} = \left\| \boldsymbol{W} \oplus \boldsymbol{P}_{I,i} \right\| \\ &\text{subject to} \quad Si \in S_{pre},\ i = 1,\ 2,... \end{aligned} \tag{37}$$

Users can adjust the values of angles α and β in the vector $\boldsymbol{W}$ according to specific control objectives. For example, in applications where limiting the cable force is critical, the angle α can be increased while the angle β is reduced. Then, the geometric layout obtained in (37) will primarily focus on reducing the maximum cable force. Each geometric layout provides specific advantages, such as shortening stabilization time, reducing maximum cable force, or using fewer cables. The geometry selection strategy leverages the characteristics of each layout of the CDR to align with different control objectives for vibration damping.

C. Case Validation

This part applies the geometry selection strategy to analyze and identify the optimized geometry of a CDR for vibration damping in a plate. The structural parameters of the 6-meter plate are listed in TABLE I. First, we define the dimensional parameters for the predefined anchor point as Δl = 1000 mm and Δw = 100 mm. In the first stage of geometry selection, this results in 42 predefined anchor points on the plate. Second, the maximum number of cables is set to 4, with the additional constraint that no more than 2 cables can be placed on any one side of the plate. By combining the first two stages of the geometry selection, a total of 624 geometry layouts are generated, meaning that the set S_{original} contains 624 elements. To avoid verbosity and complexity, this paper focuses on analyzing 16 geometric layouts of them as examples. Fig. 8 depicts these 16 layouts. The coordinates of the anchor points are provided in TABLE IV in the supplementary material.

Under the CFFF and FFFF boundary conditions, the tip displacements of the plate for the 16 geometric layouts (S1 to S16) are shown in Fig. S2 and Fig. S4, respectively. Fig. S3 and Fig. S5 illustrate the cable forces for the first four geometric layouts (S1 to S4) under both boundary conditions. Fig. S6 depicts the performance index $P_{I,i}$ under both two boundary conditions. Due to the page limit, Figs. S2-S6 are included in the supplementary material.

Under the CFFF boundary conditions, the adopted control parameters in (29) are: $\sigma_1 = 7$, $\sigma_2 = 5$, $\sigma_3 = 4$, $\sigma_4 = 0$, $\xi_1 = 15$, $\xi_2 = 10$, $\xi_3 = 5$, and $\Delta t_r = 0.4$. The value of t_r is determined based on t_{pr}, the time of the relative extremum on the vibration curve. Herein, we define that $t_r = t_{pr} + 0.4$. For the FFFF boundary condition, the control parameters are: $\sigma_1 = 6$, $\sigma_2 = 4$, $\sigma_3 = 2$, $\sigma_4 = 1$, $\sigma_5 = 0$, $\xi_1 = 35$, $\xi_2 = 25$, $\xi_3 = 15$, $\xi_4 = 5$, $t_r = t_{pr} + 0.1$, and $\Delta t_r = 0.3$. Additionally, the weight M_l = 45 kg, l_1 = 1500 mm, l_2 = 4500 mm, n_w = 13, and n_l = 121. We specify $\delta = 5$, $\delta_t = 50$ and leave no limit on δ_F. Therefore, S_{pre} = {S3, S4, S7, S8, S11, S12, S16} under the CFFF boundary condition, and S_{pre} = {S3, S4, S7, S8, S11, S12} under the FFFF boundary condition.

Under the CFFF boundary condition, for geometric layouts S5 to S16, the stabilization time gradually decreases as the anchor points approach the free end of the plate. However, in

TABLE I
PARAMETER OF THE RECTANGULAR PLATE

Symbol	Meaning	Value
l	Length of the plate	6000 mm
w	Width of the plate	600 mm
d	Thickness of the plate	12 mm
ρ	Density of the plate	1370 kg/m^3
E	Young modulus of the plate	9.5 Gpa
v	Poisson's ratio of the plate	0.28
ς_1	Damping coefficient	0.007
ς_2	Damping coefficient	0.01

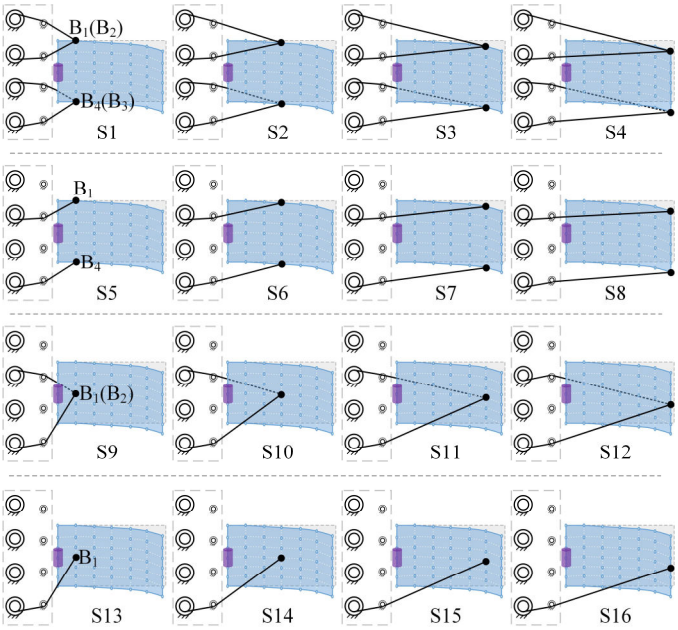

Fig. 8. Geometric layouts S1 to S16 of the CDR.

the four-cable geometric layouts S1 to S4, the stabilization time first decreases and then increases, reaching a minimum value at layout S3 (16.7s at point I). Under the FFFF boundary condition, as the anchor points approach the right end of the plate, the stabilization time for layouts S1 to S16 follows a similar pattern: it initially decreases and then increases. One consistent result between the CFFF and FFFF conditions is that layout S3 still has the shortest stabilization time (21.9 s at point VIII) among all 16 layouts.

Under both boundary conditions, the stabilization time gradually decreases as the number of cables increases. For example, under the CFFF boundary condition, the stabilization time for the four-cable layout S3 is 16.7 s. In comparison, the two-cable layout S11 has a stabilization time is 26.7 s, while the single-cable layout S15 exceeds 50.0 s. For layouts with the same number of cables, we categorize those that evenly distribute the cables on both sides of the plate as bilateral layouts (S9 to S12), and those that place all cables on the same side of the plate as unilateral layouts (S5 to S8). It is evident that, with the same number of cables, the stabilization time of unilateral layouts is longer than that of bilateral layouts. For example, the stabilization time for the unilateral layout S8 is 34.6 s, while it reduces to 24.8 s for the bilateral layout S12.

In Fig. S6, we define four sets of values for α and β as follows: 1) $\alpha=25$ and $\beta=30$: to select a layout that prioritizes

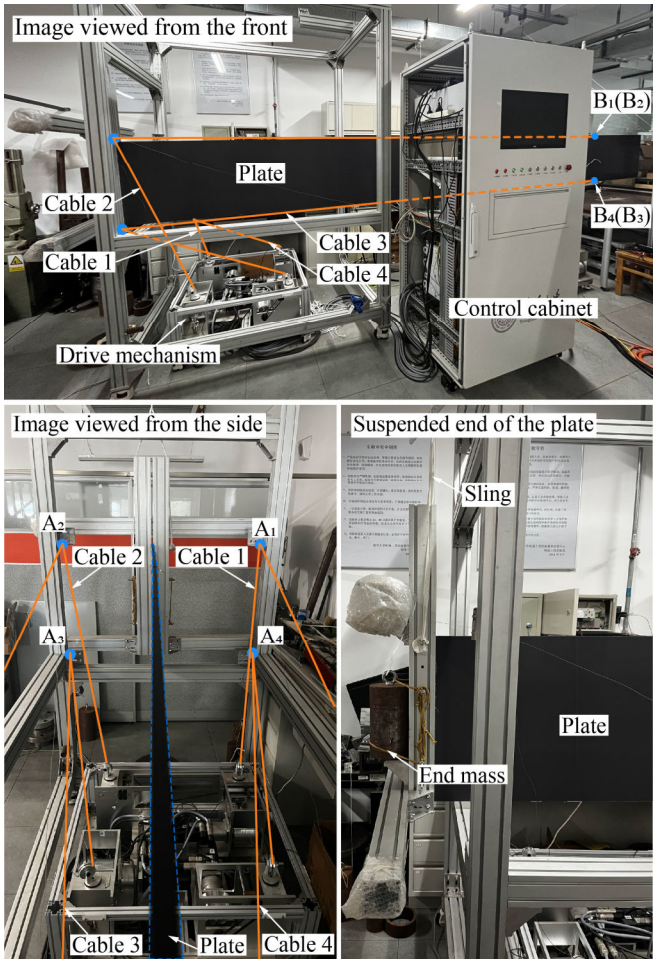

Fig. 9. Experimental setup.

shortening stabilization time; 2) $\alpha=75$ and $\beta=15$: to select a layout that focus on reducing cable forces; 3) $\alpha=70$ and $\beta=72$: to select the layout that emphasizes using fewer cables; 4) $\alpha = 54.7$ and $\beta = 45$: to select a layout with balanced performance. As shown in Fig. S6, when the primary control objective is to shorten the stabilization time ($\alpha=25$, $\beta=30$), S3 is the preferred geometric layout under both the CFFF and FFFF boundary conditions. When the focus is on reducing cable forces ($\alpha=75$, $\beta=15$), S12 becomes the preferred layout under the CFFF boundary condition, while S11 is favored under the FFFF boundary condition. When reducing the number of cables is the priority ($\alpha=70$, $\beta=72$), the preferred layout shifts to S16 under the CFFF boundary condition. Despite its longer stabilization time, S16 achieves a lower index due to its advantage of using fewer cables, which aligns with the emphasis on reducing the number of cables. Under the FFFF boundary condition, S11 remains the preferred layout. When the control objective is balanced performance, S12 is the chosen layout under the CFFF boundary condition, while S11 is preferred under the FFFF boundary condition.

V. EXPERIMENTAL RESULTS

An experimental setup (see Fig. 9) was built to validate the practical feasibility of the geometry selection strategy. It includes a dSPACE controller, Quantum M878B and M840B devices for signal acquisition, four Lenze MCS09D41 AC

motors, four HBM U9C loadcells, and KEYENCE IL600 laser sensors. To provide the CFFF boundary condition, the left side of the plate is clamped, while the other three sides remained free. For the FFFF boundary condition, the plate was suspended using three slings, with the placement of their anchor points (Q_1, Q_2, and Q_3) shown in Fig. 2. Using this setup, we formed 16 geometric layouts (S1 to S16) as illustrated in Fig. 8, under both boundary conditions.

The tip displacements under CFFF and FFFF boundary conditions are illustrated in Fig. 10 and Fig. 12, respectively. Under the FFFF boundary condition, the stabilization time for geometric layouts S1 to S16 initially decreases and then increases as the anchor points move closer to the right end. However, under the CFFF boundary condition, only the four-cable layouts S1 to S4 show this trend, while for layouts S5 to S16, the stabilization time steadily decreases as the anchor points approach the free end. In both CFFF and FFFF boundary conditions, geometric layout S3 has the shortest stabilization time among the 16 layouts (Point I: 17.8 s, Point VIII: 20.4 s). Under the FFFF boundary condition, layouts S1, S5, S9, and S13 show minimal reduction in stabilization time, with their tip displacements almost overlapping with the free vibration displacement curve. As the number of cables increases, the stabilization time gradually decreases under both CFFF and FFFF boundary conditions. This is because, within the output limit range in (30), more work is performed by more cables in the same period of time, leading to faster dissipation of vibration energy. In terms of stabilization time, bilateral layouts outperform unilateral layouts (with the same number of cables), which is consistent with simulation results. Due to the alternating output characteristic of the control input, the frequency of force output in bilateral layouts is doubled compared to unilateral layouts, allowing for more vibration energy to be dissipated in the same time period, resulting in shorter stabilization times.

The cable forces for the four-cable layouts S1 to S4 under CFFF and FFFF boundary conditions are shown in Fig. 11 and Fig. 13, respectively. A discrepancy exists between the cable tip displacements in the experimental and simulation results, partly due to differences in cable force output and partly because it is difficult to precisely replicate the actual boundary conditions in the simulation. For example, it is challenging to precisely replicate the lateral displacement constraints imposed by slings 1, 2 and 3 in the simulation model. Overall, the tip displacements in both simulations and experiments show acceptable consistency in terms of the overall trends.

In the experiment, we used the same four sets of parameters for α and β as in the simulation, and the resulting performance indices are shown in Fig. 14. When the stabilization time is the primary priority (α = 25, β = 30), the experimental results under both CFFF and FFFF boundary conditions indicate that S3 is the preferred geometric layout, which aligns with the simulation results. When the maximum cable force is the first priority (α = 75, β = 15), experimental results under the CFFF boundary condition suggest that S11 is the preferred layout, while the corresponding optimized layout in the simulation is S12. Under FFFF boundary conditions, the experimental results point to S12 as the optimized layout, whereas the simulation favors S11. Since S11 and S12 are double-cable bilateral layouts with relatively close anchor points and high similarity, they can both be considered optimized geometric layouts when reducing cable force is the main concern. When the number of cables is the primary priority (α=70, β=72), both simulation and experimental results under CFFF boundary conditions identify S16 as the optimized geometry.

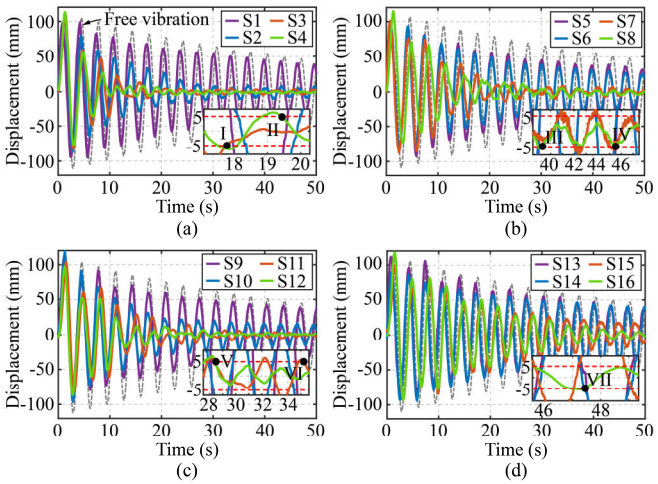

Fig. 10. Tip displacement of the plate under the CFFF boundary condition. (a) S1 to S4. (b) S5 to S8. (c) S9 to S12. (d) S13 to S16.

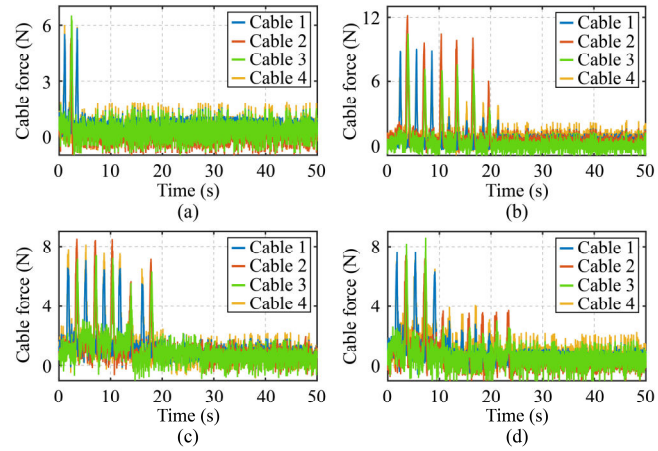

Fig. 11. Cable force in experiments under the CFFF boundary condition. (a) S1. (b) S2. (c) S3. (d) S4.

TABLE II
VIBRATION DAMPING DATA OF 16 GEOMETRIES UNDER CFFF CONDITION

Geometry	Maximum cable force (N)					Stabilization time (s)		Number of cables
	Experiment				Simulation	Experiment	Simulation	
	F_1	F_2	F_3	F_4	$F_1/F_2/F_3/F_4$			
S1	5.8	5.3	6.5	6.0	4.0	>50.0	>50.0	4
S2	8.9	12.2	10.5	7.9	7.0	>50.0	>50.0	4
S3	6.9	8.5	7.4	8.1	7.0	17.8	16.7	4
S4	7.6	7.4	8.6	7.1	7.0	19.4	18.4	4
S5	8.1	-	-	8.0	4.0	>50.0	>50.0	2
S6	8.4	-	-	6.7	5.0	>50.0	>50.0	2
S7	9.6	-	-	10.4	7.0	45.5	38.3	2
S8	9.6	-	-	11.5	7.0	39.3	34.6	2
S9	3.9	2.2	-	-	4.0	>50.0	>50.0	2
S10	10.3	11.3	-	-	7.0	>50.0	>50.0	2
S11	7.5	8.4	-	-	7.0	35.1	26.7	2
S12	7.7	9.3	-	-	7.0	28.4	24.8	2
S13	7.2	-	-	-	4.0	>50.0	>50.0	1
S14	8.2	-	-	-	7.0	>50.0	>50.0	1
S15	8.7	-	-	-	7.0	>50.0	>50.0	1
S16	9.6	-	-	-	7.0	47.4	43.4	1

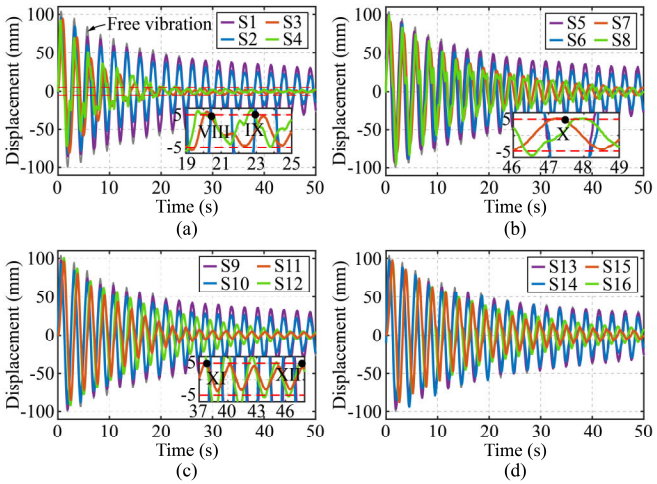

Fig. 12. Tip displacement of the plate under the FFFF boundary condition. (a) S1 to S4. (b) S5 to S8. (c) S9 to S12. (d) S13 to S16.

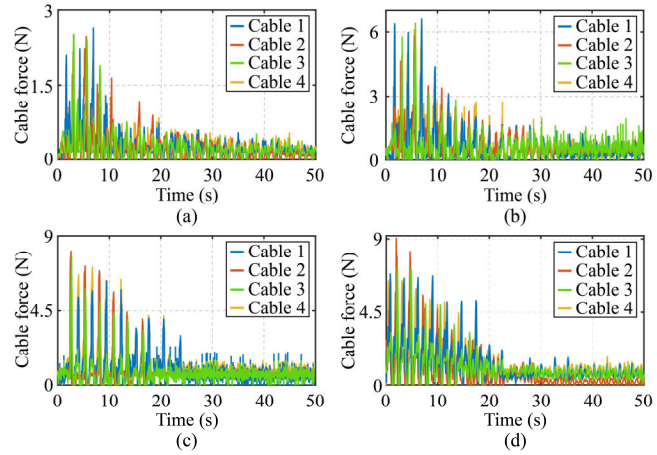

Fig. 13. Cable force in experiments under the FFFF boundary condition. (a) S1. (b) S2. (c) S3. (d) S4.

TABLE III
VIBRATION DAMPING DATA OF 16 GEOMETRIES UNDER FFFF CONDITION

Geometry	Maximum cable force (N)					Stabilization time (s)		Number of cables
	Experiment				Simulation	Experiment	Simulation	
	F_1	F_2	F_3	F_4	$F_1/F_2/F_3/F_4$			
S1	2.6	2.5	2.5	2.1	2.0	>50.0	>50.0	4
S2	6.6	5.8	6.4	6.3	4.0	>50.0	>50.0	4
S3	6.3	8.1	7.7	7.1	6.0	20.4	21.9	4
S4	6.9	9.0	7.2	6.7	6.0	22.9	23.2	4
S5	2.6	-	-	2.5	2.0	>50.0	>50.0	2
S6	5.3	-	-	6.1	4.0	>50.0	>50.0	2
S7	6.0	-	-	5.1	6.0	47.7	39.7	2
S8	6.2	-	-	5.4	6.0	51.8	39.8	2
S9	2.7	2.6	-	-	2.0	>50.0	>50.0	2
S10	6.3	6.9	-	-	4.0	>50.0	>50.0	2
S11	7.4	7.4	-	-	6.0	37.8	34.6	2
S12	5.4	5.9	-	-	6.0	47.7	35.8	2
S13	2.8	-	-	-	2.0	>50.0	>50.0	1
S14	7.1	-	-	-	4.0	>50.0	>50.0	1
S15	8.2	-	-	-	6.0	>50.0	>50.0	1
S16	6.6	-	-	-	6.0	>50.0	>50.0	1

Under the FFFF boundary condition, both simulation and experimental results prefer S11. When the control objective aims for balanced performance (α = 54.7 and β = 45), both simulation and experimental results under CFFF boundary conditions suggest S12 as the optimized layout, while under

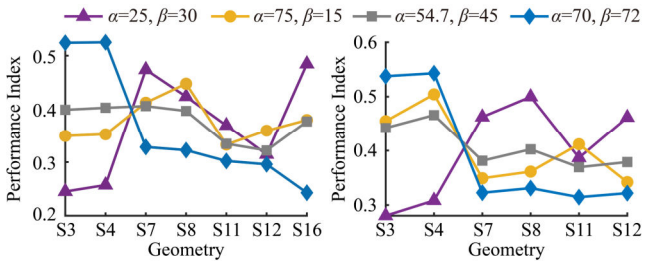

Fig. 14. Performance index $P_{I,i}$. (a) Under the CFFF boundary condition. (b) Under the FFFF boundary condition.

FFFF conditions, S11 is preferred in both. Combining these simulation and experimental findings, it is evident that the proposed geometry selection strategy effectively identifies optimized geometric layouts for different control objectives. These layouts demonstrate clear advantages in the experimental results, verifying the practical feasibility and the accurate screening ability of the strategy.

VI. CONCLUSION

This work proposed a comprehensive geometry selection strategy to enhance vibration damping of plates using CDRs. The strategy directly incorporates closed-loop control behaviors and simultaneously considers stabilization time, control input constraints, and the number of cables. By introducing a normalized weighting vector, the strategy provides geometries tailored to diverse control objectives, such as achieving faster stabilization or reducing cable forces. Drawing on the output characteristics of the designed DRLBC, a new control law with customizable functions is developed, allowing for flexible output force modulation and ensuring effective vibration damping. Under both CFFF and FFFF boundary conditions, the selection strategy provided preferred geometric layouts aligned with specific control objectives. We validated the strategy on a six-meter-scale experimental platform, constructing 16 geometric layouts and comparing their vibration-damping performance under both boundary conditions. The results demonstrated that the strategy effectively identified preferred geometries for different control objectives, with experiments highlighting clear advantages of the selected geometries and confirming the practical feasibility and accurate screening ability of the strategy.

REFERENCES

[1] Y. Li, J. Onoda, and K. Minesugi, "Simultaneous optimization of piezoelectric actuator placement and feedback for vibration suppression," *Acta Astronaut.*, vol. 50, pp. 335–341, 2002.
[2] D. J. Phillips, D. C. Hyland, and E. G. Collins, "Experimental demonstration of active vibration control for flexible structures," in *Proc. IEEE Conf. Decis. Control (IEEE CDC)*, 1990, pp. 2024–2029.
[3] J. N. Juang, "Optimal design of a passive vibration absorber for a truss beam," *J. Guid. Control Dyn.*, vol. 7, no. 6, pp. 733–739, 1984.
[4] A. Kras and P. Gardonio, "Velocity feedback control with a flywheel proof mass actuator," *J. Sound Vibr.*, vol. 402, pp. 31–50, 2017.
[5] S. Matunaga, Y. Yu, and Y. Ohkami, "Vibration suppression using acceleration feedback control with multiple proof-mass actuators," *AIAA J.*, vol. 35, no. 5, pp. 856-862, 1997.
[6] J. F. Shi and C. J. Damaren, "Control law for active structural damping using a control moment gyro," *J. Guid. Control Dyn.*, vol. 28, no. 3, pp. 550–553, 2005.
[7] G. Zhang, J. Furusho, and M. Sakaguchi, "Vibration suppression control of robot arms using a homogeneous-type electrorheological fluid,"

IEEE-ASME Trans. Mechatron., vol.5, no. 3, pp. 302–309, 2000.
[8] H. U. Oh and J. Onoda, "An experimental study of a semiactive magneto-rheological fluid variable damper for vibration suppression of truss structures," *Smart Mater. Struct.*, vol. 11, pp. 156–162, 2002.
[9] B. Yang, Z. Fan, J. Miao *et al.*, "Active vibration control of flexible satellites using solid propellant microthruster array," *J. Aerosp. Eng.*, vol. 31, no.2, pp. 04017092-1–04017092-12, 2018.
[10] F. Casella, A. Locatelli and N. Schiavoni, "Nonlinear controllers for vibration suppression in a large flexible structure," *Control Eng. Practice*, vol. 4, no. 6, pp. 791–806, 1996.
[11] M. Allen, F. Bernelli-Zazzera, and R. Scattolini, "Sliding mode control of a large flexible space structure," *Control Eng. Practice*, vol. 8, no. 8, pp. 861–871, 2000.
[12] H. T. Zhang, Z. Chen, P. Chen *et al.*, "Saturated output regulation approach for active vibration control of thin-walled flexible workpieces with voice coil actuators," *IEEE/ASME Trans. Mechatron.*, vol. 21, no.1, pp. 266–275, 2015.
[13] E. F. Crawley and J. De Luis, "Use of piezoelectric actuators as elements of intelligent structures," *AIAA J.*, vol. 25, no. 10, pp. 1373–1385, 1987.
[14] J. K. Hwang, C. H. Choi, C. K. Song, and J. M. Lee, "Robust LQG control of an all-clamped thin plate with piezoelectric actuators/sensors," *IEEE/ASME Trans. Mechatron.*, vol. 2, no. 3, pp. 205–212, 1997.
[15] Q. Hu, Y. Jia, and S. Xu, "Dynamics and vibration suppression of space structures with control moment gyroscopes," *Acta Astronaut.*, vol. 96, pp. 232–245, 2014.
[16] W. Gawronski, "Actuator and sensor placement for structural testing and control," *J. Sound Vibr.*, vol. 208, no. 1, pp. 101–109, 1997.
[17] Z. Qiu, X. Zhang, H. Wu, and H. Zhang, "Optimal placement and active vibration control for piezoelectric smart flexible cantilever plate," *J. Sound Vibr.*, vol. 301, pp. 521–543, 2007.
[18] N. D. Zorić, A. M. Tomović, A. M. Obradović *et al.*, "Active vibration control of smart composite plates using optimized self-tuning fuzzy logic controller with optimization of placement, sizing and orientation of PFRC actuators," *J. Sound Vibr.*, vol. 456, pp. 173–198, 2019.
[19] A. Nadi, M. Mahzoon, and E. Azadi Yazdi, "Optimal distribution of piezoelectric patches for active vibration reduction of a thick plate using singular value decomposition approach," *Sci Rep*, vol. 11, no. 1, pp. 13721, 2021.
[20] D. Halim and S. O. R. Moheimani, "An optimization approach to optimal placement of collocated piezoelectric actuators and sensors on a thin plate," *Mechatronics*, vol. 13, pp. 27–47, 2003.
[21] L. F. Yang, M. M. Mikulas Jr, K. C. Park *et al.*, "Slewing maneuvers and vibration control of space structures by feedforward/feedback moment-gyro controls," *J. Dyn. Syst. Meas. Control-Trans. ASME*, vol. 117, pp. 343–351, 1995.
[22] S. A. Chee, "Vibration suppression of large space structures using an optimized distribution of control moment gyros," Toronto, ON, Canada: University of Toronto, 2011, pp. 35–38.
[23] Z. Wang and T. Li, "Optimal Piezoelectric sensor/actuator placement of cable net structures using H_2-norm measures," *J. Vib. Control*, vol. 20, no. 8, pp. 1257–1268, 2014.
[24] C. Spier, J. C. Bruch Jr, J. M. Sloss *et al.*, "Placement of Multiple Piezo Patch Sensors and Actuators for a Cantilever Beam to Maximize Frequencies and Frequency Gaps," *J. Vib. Control*, vol. 15, no. 5, pp. 643–670, 2009.
[25] A. G. A. Muthalif, K. A. M. Nor, A. N. Wahid *et al.*, "Optimization of piezoelectric sensor-actuator for plate vibration control using evolutionary computation: Modeling, simulation and experimentation," *IEEE Access*, vol. 9, pp. 100725–100734, 2021.
[26] Y. Sun, Z. Song, and F. Li, "Theoretical and experimental studies of an effective active vibration control method based on the deflection shape theory and optimal algorithm," *Mech. Syst. Signal Proc.*, vol. 170, pp. 108650, 2022.
[27] F. Angeletti, P. Iannelli, P. Gasbarri *et al.*, "End-to-end design of a robust attitude control and vibration suppression system for large space smart structures," *Acta Astronaut.*, vol. 187, pp. 416–428, 2021.
[28] T. Wu, Z. Chen, H. Yan *et al.*, "Optimization of the location of piezoelectric actuator and sensor in active vibration control using Multi-Verse Optimizer algorithm," *J. Intell. Mater. Syst. Struct.*, vol. 34, no. 4, pp. 401–414, 2023.
[29] T. Zhao, W. Tian, H. Wang *et al.*, "Optimized placement of piezoelectric actuator for multichannel adaptive vibration control of a stiffened plate," *J. Aerosp. Eng.*, vol. 35, no. 1, pp. 04021102, 2022.
[30] F. Botta, A. Rossi, and N. P. Belfiore, "A novel method to fully suppress single and bi-modal excitations due to the support vibration by means of piezoelectric actuators," *J. Sound Vibr.*, vol. 510, pp. 116260, 2021.
[31] X. Wang, W. Zhou, Z. Wu *et al.*, "Integrated design of laminated composite structures with piezocomposite actuators for active shape control," *Compos. Struct.*, vol. 215, pp. 166–177, 2019.
[32] B. Prakash, M. Y. Yasin, A. H. Khan *et al.*, "Optimal location and geometry of sensors and actuators for active vibration control of smart composite beams," *Aust. J. Mech. Eng.*, vol. 20, no. 4, pp. 981–999, 2022.
[33] D. Piron, S. Pathak, A. Deraemaeker *et al.*, "A pole-zero based criterion for optimal placement of collocated sensor-actuator pair," *Mech. Syst. Signal Proc.*, vol. 155, pp. 107533, 2021.
[34] M. Rakotondrabe, C. Clévy, and P. Lutz, "Complete open loop control of hysteretic, creeped, and oscillating piezoelectric cantilevers," *IEEE Trans. Autom. Sci. Eng.*, vol. 7, no. 3, pp. 440–450, 2009.
[35] W. He, T. Meng, X. He, *et al.*, "Unified iterative learning control for flexible structures with input constraints," *Automatica*, vol. 96, pp. 326-336, 2018.
[36] X. Wang, B. Zhang, W. Shang, F. Zhang, and S. Cong, "Constrained path planning for reconfiguration of cable-driven parallel robots," *IEEE/ASME Trans. Mechatron.*, vol. 28, no. 4, pp. 2352–2363, 2023.
[37] H. Jia, W. Shang, F. Xie, B. Zhang, and S. Cong, "Second-order sliding-mode-based synchronization control of cable-driven parallel robots," *IEEE/ASME Trans. Mechatron.*, vol. 25, no. 1, pp. 383–394, 2019.
[38] K. J. Bathe, Finite Element Procedures. Watertown, MA, USA: K.J. Bathe, 2019, 2nd ed., sixth printing, ISBN 978-0-9790049-5-7, pp. 80, 136, 151, 347–348, 424.
[39] D. L. Logan, A First Course in the Finite Element Method. Toronto, ON, Canada: Nelson, 2007, 4th ed., ISBN 0-534-55298-6, pp. 28–39, 515–523.
[40] T. P. Lillicrap, J. J. Hunt, A. Pritzel, *et al.*, "Continuous control with deep reinforcement learning," arXiv preprint arXiv:1509.02971, 2015.
[41] Q. Song, J. Shi, Z. Liu, *et al.*, "Dynamic analysis of rectangular thin plates of arbitrary boundary conditions under moving loads," *Int. J. Mech. Sci.*, vol. 117, pp. 16–29, 2016.
[42] K. J. Bathe and E. L. Wilson, "Stability and accuracy analysis of direct integration methods," *Earthq. Eng. Struct. Dyn.*, vol. 1, no. 3, pp. 283–291, 1972.

Haining Sun (Member, IEEE) received the B.Eng. degree in mechanical engineering from Shandong University, Jinan, China, in 2017, and the Ph.D. degree in mechanical engineering from Tsinghua University, Beijing, China, in 2022. He is currently with the Singapore Institute of Manufacturing Technology, Singapore. His current research interests include cable-driven robots, vibration control, dynamic control, and force control.

Shuzhi Sam Ge (Fellow, IEEE) received the B.Sc. degree from the Beijing University of Aeronautics and Astronautics, Beijing, China, in 1986, and the Ph.D. degree from the Imperial College London, London, U.K., in 1993.

He is a fellow of SAEng, IEEE, IFAC, IET and CAA, Professor with the Department of Electrical and Computer Engineering, PI Member of Institute for Functional Intelligent Materials, the National University of Singapore. Founder of Institute for Future (IFF), Qingdao University, China. He Serves as President Elect of Asian Control Association, 2022-2024, IFAC executive officers as Council Member, 2023-2026, Steering Committee Chair of International Conference on Social Robotics. He served as Vice President of Technical Activities and Membership Activities, 2009-2012, Member of Board of Governors, 2007-2009, and Chair of Technical Committee on Intelligent Control, 2005-2008, of IEEE Control Systems Society. He was the recipient of many awards including National Technology Award from Singapore, IEEE Control Systems Society Distinguished Member Award, AI Grand Challenge Award from AI SG. His research interests include robotics, intelligent systems, and intelligent materials. He has (co)-authored nine books, and over 800 international journal and conference papers, with high H index (110) and citations (58,000).